WIND ENERGY
Wind Energ. (2012)
Published online in Wiley Online Library (wileyonlinelibrary.com). DOI: 10.1002/we.539

RESEARCH ARTICLE

Coherent Doppler lidar for wind farm characterization

R. Krishnamurthy[1], A. Choukulkar[1], R. Calhoun[1], J. Fine[2], A. Oliver[2] and K.S. Barr[3]

[1] Environmental Remote Sensing Group, Arizona State University, Tempe, AZ, USA
[2] Renewable Energy Systems Americas Inc., CO, USA
[3] Lockheed Martin Coherent Technologies, Inc., Louisville, CO, USA

ABSTRACT

Coherent Doppler lidar measurements are of increasing interest for the wind energy industry. Wind measurements are fundamental inputs for the evaluation of potential energy yield and performance of wind farms. Three-dimensional scanning Doppler lidar may provide a new basis for wind farm site selection, design and optimization. In this paper, the authors discuss Doppler lidar measurements obtained for a wind energy development. The possibility of using lidar measurements to more fully characterize the wind field is discussed, specifically terrain effects, spatial variation of winds, power density and the effect of shear at different layers within the rotor swept area. Vector retrieval methods have been applied to the lidar data, and results are presented on an elevated terrain-following surface at hub height. The vector retrieval estimates are compared with tower measurements, after interpolation to the appropriate level. Doppler lidar data are used to estimate the spatial power density at hub height (for the period of the deployment). An example wind farm layout is presented for demonstration purposes based purely on lidar measurement, even though the lidar data acquisition period cannot be considered climatological. The strength of this approach is the ability to directly measure spatial variations of the wind field over the wind farm. Also, because Doppler lidar can measure winds at different vertical levels, an approach for estimating wind power density over the rotor swept area (rather than only the hub height) is explored. Finally, advanced vector retrieval algorithms have been applied to better characterize local wind variations and shear. Copyright © 2012 John Wiley & Sons, Ltd.

KEYWORDS

Doppler lidar; power density; spatial wind distribution; wind energy; wind farm layout

Correspondence

Raghavendra Krishnamurthy, Mechanical and Aerospace Engineering, Arizona State University, Main Campus, PO Box 876106, Tempe, AZ 85287-6106, USA.
E-mail: raghavendr.Krishnamurthy@asu.edu

Received 24 March 2011; Revised 27 September 2011; Accepted 5 October 2011

1. INTRODUCTION

Wind energy is one of the fastest growing and currently practical forms of renewable energy.[1] Reliable measurement of wind fields is an important foundation of optimal design and operation of wind farms. Current industry standards for wind and turbulence measurements for wind energy applications are to utilize in-situ wind instruments, most typically cup and vane anemometers on tall meteorological masts.[2,3] For the latest large turbine models, conventional mast wind speed measurements are insufficient, and installations of high mast wind speed measurements are problematic because of cost and safety considerations. There is a growing awareness of the inadequacy of current methods to measure the spatial variability of the winds, both vertically and horizontally, for wind assessment.[4,5] Because of the global growth of wind energy, short-range lidar profilers, sodars are proliferating and are increasingly being used to measure wind profiles.[6–8] A larger body of open literature is required to more fully understand the character of these and other remote sensing measurements for wind energy applications. 3D coherent Doppler lidars have been extensively used in meteorological studies for the past few decades.[9–12] Modern 3D scanning coherent Doppler lidars are well suited for characterizing wind farm airsheds and may eventually form a new basis for real-time adaptive control of wind turbines.[13] Lidars can measure the velocity deficit downstream of an individual wind turbine,[14] as well as the accumulated wakes from an array of turbines. Typical ranges of the current generation of commercially available coherent Doppler lidar (such as that used in this study, i.e. *WindTracer*, from *Lockheed Martin Coherent Technologies, Inc.*) are 10–20 km, depending on the atmospheric conditions.

Previous wind energy literature has already emphasized the importance of obtaining and utilizing more complete information from the wind profile. For example, Wagner *et al.*[15] suggest that more accurate power curves can be obtained by replacing the single wind speed at hub height with *effective wind speeds* that account for the vertical variability of the wind profile over the rotor plane. In addition, identification of complex flow phenomena such as nocturnal jets[16] or periodic shear instabilities[17] is critical for normal operation of wind turbines. These flow events can be difficult to adequately capture with tower measurements alone.

In order to understand how wind profiles are obtained by lidar, it is useful to review the difference between the fundamental measured product of the Doppler lidar and secondary retrieved products. Doppler lidars fundamentally measure a Doppler shift along their laser beam propagation path. Therefore, motion of the air orthogonal to the propagation path of the laser beam produces no Doppler shift. Consequently, the basic Doppler lidar output is the *radial velocity* or the dot product of the velocity vector with the beam direction unit vector. Interpretation and processing of the radial velocity fields can be complex, requiring the resolution of indeterminacy in the basic data through supplementary assumptions or information. Various wind retrieval techniques have been developed to estimate 2D and 3D vector fields from Doppler lidar data.[10,18–21] Algorithms range from computationally intensive 4DVAR (four-dimensional variational data assimilation) techniques to simpler and faster methods based on volume velocity processing (VVP)[4,22] and 2DVAR.[18] Current techniques are generally suitable for many applications such as pollution transport studies and vertical profiling for wind farms assuming that the averaged nature of the products and underlying assumptions are understood. Dual Doppler lidar techniques also provide accurate estimates of the 2D wind field.[23–26]

The flexibility of lidar to perform conical [plan position indicator (PPI)], vertical-slice (range height indicator) or fixed-beam measurements allows investigation of a variety of boundary layer characteristics. The wind-field structure from different points of view can be visualized, e.g., mean wind and turbulent profiles, time series or as images of individual scans, to reveal flow features at hub height and above the range of tower measurements. Evidence will be presented later that *3D scanning coherent Doppler lidar is also capable of producing wind speed distribution of the wind field as a function of space*. This can be used to obtain a spatial power density distribution over the entire region. This paper presents the results of a Doppler lidar deployment for a proposed wind energy development. The objectives of this paper are as follows:

- To characterize the spatial wind field at the hub height over the entire region
- To calculate (spatially varying) wind speed distribution and spatial power density distribution over the region of interest
- To estimate power density using multiple vertical layers within the rotor swept area
- To demonstrate a simple algorithm for wind farm layout design based on spatial power density distribution and distance limitation
- Apply advanced optimal interpolation retrieval algorithms to lidar data

2. LIDAR STUDY

The Doppler lidar used in this study was a 2 μm eye safe *WindTracer* lidar manufactured by *Lockheed Martin Coherent Technologies, Inc.* (Louisville, Co, USA).[27,28] The lidar was located at the center of the region of interest. The site provided excellent 360° line of sight and clear views to all locations within the wind farm (Figure 1). The initial range observed was from 8 to 12 km depending on averaging and atmospheric conditions. The lidar has an initial blind zone of 436 m (i.e., the backscatter from this zone is not detectable by lidar), over which no data is collected (shown as grey region surrounding the lidar). The location of the study is confidential as it is a part of an ongoing wind energy assessment study for a commercial enterprise. The study was conducted during the months of June and July in 2007.

2.1. Lidar parameters and scanning strategy

A coherent Doppler lidar estimates the radial velocity of the collection of aerosol particles illuminated by the lidar pulse as it travels through the atmosphere. The performance of Doppler lidars depends on the parameters, the atmospheric conditions and the velocity estimation algorithm.[11,26] Table I provides the coherent Doppler lidar parameters utilized during this study. The lidar utilizes a Gaussian pulse with a width of 105 m (full width at half maximum).[11] For this experiment, the range-gate length (distance between two radial measurements) was set at 105 m, and an azimuthal scanning rate of 9.55° s^{-1} was used. As this type of lidar has a pulse repetition frequency of 500 Hz, 100 lidar pulses averaging produced 'beams' of data every 0.2 s. Therefore, the azimuthal spacing between beam products was $\Delta\phi = 1.96°$. The horizontal resolution between two successive measurements is approximately 17 m, at the first range gate, to 205 m, at farthest range gate (due to diverging beams). The vertical resolution between successive elevation angles was approximately 18 m (at the farthest range gate). The accuracy for this type of lidar was expected to be in the range of 0.1–0.5 m s^{-1} for the radial velocity product beams.[11]

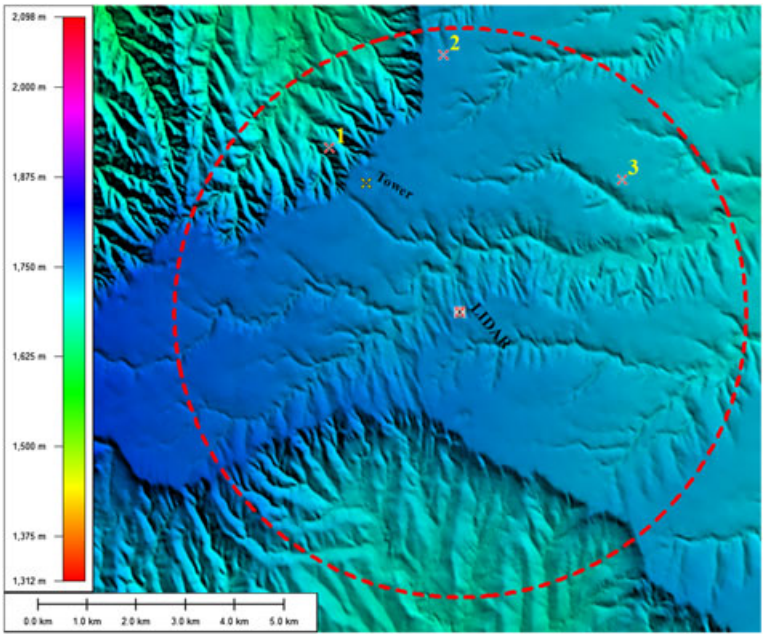

Figure 1. The terrain of the site study (oriented facing north). The position of the lidar (center) and the tower (north of lidar) is shown. The lidar scan radius is shown (dotted red line), and 1, 2 and 3 (cross marks) are locations where different wind speed distributions were observed (discussed in Section 5.2).

Table I. Characteristics of the Doppler lidar system.

Transmitter	Nd-Yag
Operating wavelength	2 μm
Energy per pulse	2 mJ
Pulse repetition	500 Hz
Range resolution	105 m
Min range	436 m
Max range	10,917 m

Because of the complex terrain, a set of different simple scans were assembled so that data could be obtained on a terrain-following surface at hub height. The data were acquired for a period of 1 month. A stack of 360° PPIs with varying elevation angles (0.05°, 0.24°, 0.43°, 0.62°, 0.81°, 1.0°, 1.19°, 1.45°, etc.) were performed to measure data for the majority of the domain. The elevation angles were chosen to acquire radial wind velocity data above and below the hub height across the site. Data from 16 PPI scans (i.e., one stack) were used to produce the terrain-following wind speed maps. Each stack required approximately 10 min to complete. Cup anemometers and vanes were placed on a tower within the region of interest (northwest of lidar location, $\sim 325°$) to evaluate the accuracy of wind speed retrievals.

2.2. Data filtering

Data filtering is performed prior to analysis. Since the accuracy of lidar measurements decreases with increasing range due to decreasing signal-to-noise ratio (SNR), the first step in the filtering was to remove data with an SNR below −10 dB. The second filtering step is based on the relative jump of the radial velocity value compared with the previous and following data points. If the jump recorded is more than a threshold value (5 m s^{-1}) in any direction, the data point is not considered for analysis. The threshold value is generally set to separate the noise from the data and must be subjectively determined because of the individual variations associated with different datasets. Third, hard target returns (i.e., when the laser pulse hits an opaque object such as terrain) were also removed on the basis of the high SNR (> 20 dB).

3. WIND SPEED RETRIEVAL

Since the basic Doppler lidar output is the *radial velocity*, interpretation and processing of the radial velocity fields can be complex, requiring the resolution of indeterminacy in the basic data through supplementary assumptions or information.

Two advanced velocity retrieval algorithms were applied to the dataset. VVP algorithm was applied to estimate the winds on a terrain-following surface at hub height. The *terrain-following surface at hub height* is constructed by adding a vertical offset (in our case 80 m) to the surface that defines ground level over the domain. Advanced optimal interpolation technique was used to characterize atypical wind flow events.

3.1. Volume velocity processing

For the tangential components of the wind for a given radial direction and range to be estimated, adjacent lidar beam measurements are used. The VVP algorithm estimates the horizontal vector that represents the localized mean wind at the specified range gate location on a conical scan.[29,30]

The VVP algorithm first groups the obtained lidar data from the volume of scans into small conical analysis volumes.[30] The basic assumption of the VVP method is that the spatial variation of the wind within the analysis volume $\Delta r \times \Delta\Phi \times \Delta\alpha$ can be approximated by a linear function. Radial velocity data collected in the analysis volume span from r to $\mathrm{r} + \Delta\mathrm{r}$, azimuth from Φ to $\Phi + \Delta\Phi$ and elevation angle from α to $\alpha + \Delta\alpha$. Each of these volumes uses 30 to 40 radial velocity data points, depending on the size of the conical analysis volume. The VVP estimates are dependent on the size of the analysis volume. The number of radial velocity data points in each analysis volume needs to be carefully considered for converged solution. Large analysis volumes contain more radial velocity data points, but the wind field estimates become questionable because of violation of the linear wind assumption.[29] On the other hand, with too few radial velocity points, the solution can become unstable, which increases the relative error in wind speed estimates.[31] The bias in wind speed for different sector sizes for similar radar analysis is estimated to be approximately between 0.5 and 1 m s^{-1}.[31] Therefore, through trial and error, the size of the analysis volume was chosen as $\Delta r = 210$ m, $\Delta\Phi = 20°$ and $\Delta\alpha = 0.2°$. For the given unit analysis volume, the algorithm automatically loops through all analysis volumes, applying a least squares minimization scheme to obtain the solutions. Once the wind speeds are obtained for the volume of scans, they are placed in the center of the analysis volume. Wind speeds above the maximum velocity threshold (> 25 m s^{-1}) of the lidar are ignored.

3.2. Optimal interpolation

Data assimilation techniques attempt to estimate the state of the atmosphere by combining observations with an *a priori* estimate. The optimal interpolation algorithm based on data assimilation technique by Xu[32,33] was adapted to work with Doppler lidar data.[21] This technique involves importing observations into a prediction model to find an analysis field that is most consistent with the observations. The analysis field is defined as background plus the weighted innovation

$$\text{Analysis} = \text{Background} + \text{W} \times \text{Innovation} \tag{1}$$

where Innovation = Observation − Background and W is the weighting function that is a combination of the background error covariance matrix and the observation error covariance matrix.[34] This weighting is estimated based on Bayesian statistics,[35,36] which takes into account the possibility of errors in the observations. In this method, we use probabilities to estimate the confidence in knowledge of past data (background), and these probabilities are modified in light of new knowledge (observations). For this paper, simple velocity azimuth display[37] retrieval from lidar data works well as background.

The new analysis estimate is calculated by adding an analysis increment to the background. This analysis increment is estimated by minimizing the following cost function:

$$J = \Delta\boldsymbol{a}^{\mathsf{T}}\mathbf{B}^{-1}\Delta\boldsymbol{a} + (\Delta\boldsymbol{a} - \boldsymbol{d})^{\mathsf{T}}\mathbf{R}^{-1}(\Delta\boldsymbol{a} - \boldsymbol{d}) \tag{2}$$

where $\Delta\boldsymbol{a}$ is the analysis increment, given by

$$\Delta\boldsymbol{a} = \boldsymbol{x}^{\mathrm{b}} - \boldsymbol{x} \tag{3}$$

where $\boldsymbol{x}^{\mathbf{b}}$ is the background vector field and $\boldsymbol{x}$ is the analyzed vector field. $\boldsymbol{d}$ is the innovation field, and $\mathbf{B}$ and $\mathbf{R}$ are the background error covariance and observation error covariance matrices, respectively, in equation 2.

These error covariance matrices cannot be evaluated directly as this would require knowledge of the true velocity fields. Therefore, a technique known as the representer method[33] is used to evaluate these matrices and hence the velocity increment. An important assumption made in deriving the error covariance functions is that the plane of the scan is approximately horizontal. Therefore, this method works best for scans with elevation angles of less than 5° with the horizontal. Kongara *et al.*[21] presents a detailed description of the representer method and its application for the case of a Doppler lidar.

3.3. Interpolation of winds to hub height

Winds obtained from the VVP algorithm at different heights are used to generate a terrain-following wind map at hub height. At each grid point, there are normally 13 velocity values at different heights that can be used to interpolate speeds to the appropriate level. However, because of the terrain-blocking at lower levels of the lidar scans and noise caused by atmospheric conditions, the required scan levels were not always available. For this problem to be overcome, three different techniques were used to complete the interpolation:

- At grid points where there are at least two available data points at different heights, and the interpolating level is in-between these data, a linear interpolation is used to obtain the wind speed.
- At grid points where there are at least two available data points at different heights, but the interpolating level is below these data, wind speed at that level is obtained using the theoretical wind power law,[38] with locally adjusted exponent value. The exponent value is calculated on the basis of the velocity measurements available at the higher level scans.
- At grid points where there is only one available data point in the vertical direction, the interpolating level is obtained by using the wind power law,[38] where the power law exponent from the previous time period is used, assuming no change in atmospheric conditions. The time period between instances where wind speed data were available only at one vertical level was short ($\leq$ 20 min). The stability conditions are not expected to change within the short period.

This procedure is applied for the entire period of observation, and the results are provided in Section 5. Figure 2 shows the percentage of power law used at various locations during the entire period of study. Note that for 90% of the dataset, the power law is not required to estimate winds on the terrain-following surface. For locations, at the northwest and southwest ridges, where the terrain 'dips' below the horizon, extrapolation of winds onto the terrain-following surface is performed using power law. The maximum extrapolation distance used in power law calculations is approximately 20 m (as shown in Figure 3). The stability (power law exponent, α) is estimated at every grid point on the basis of winds measured at different vertical levels. The errors associated from the usage of power law should be a subject of further research. The use of power law can be assumed viable for this case, since the extrapolation distance used is small and local stability conditions are used in calculating the winds at the interpolating level.

4. DATA VALIDATION

Near continuous wind measurements were collected over a period of 1 month. Two cup anemometers and vanes were positioned at 50, 50.2 and 48 m, respectively, on a meteorological tower (location shown in Figure 1). An analysis of the measurements was performed to check their value in comparison with lidar measurements. A detailed error analysis other than the given validation with tower data of the VVP retrieval algorithm is a subject of further study.

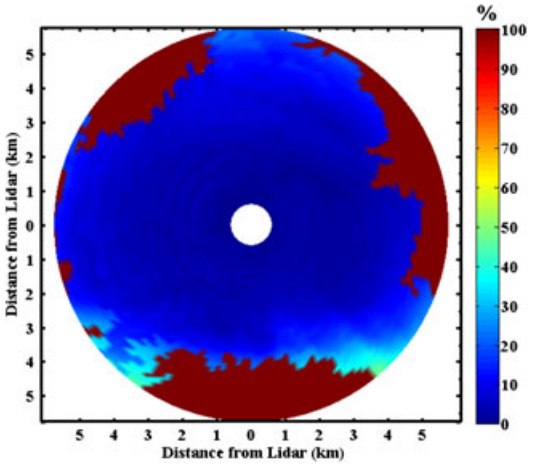

Figure 2. Percentage of power law used to obtain an 80 m terrain-following surface from lidar measurements. The color bar represents the percentage of power law used over the entire period of study. A total of 3459 observations were included for this analysis.

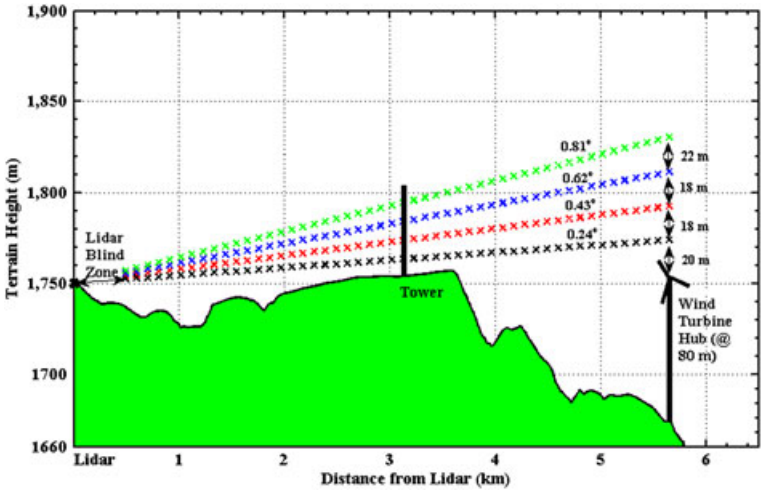

Figure 3. Terrain cross section from lidar location, through the tower, to the end of scan radius is shown. Lidar (x) and tower locations are shown. Scans at various elevation angles are displayed. The power law 'dip' height used to estimate wind speed at terrain-following surface (80 m hub height) is approximately 20 m.

4.1. Tower comparison

The lidar measurements are interpolated to 50 m above ground level (AGL) and are compared with tower measurements for the entire period of observation. The 10 min integrated mean wind speeds/directions and standard deviations for both the tower and lidar measurements are presented in Tables II and III, respectively. The time series plots of wind speed and direction for tower and lidar are shown in Figure 4. It can be seen that the lidar and tower measurements are in close agreement with the mean wind differences equal to 0.06 m s^{-1}. The 10 min root mean square (RMS) error between the lidar and the tower is estimated to be approximately 1.18 m s^{-1}. Because of the inherent differences in the data acquisition method, particularly the sampling frequency (over 10 min period: 1200 tower measurements versus one lidar measurement), the RMS differences are dependent on the averaging time period. That is, increasing averaging times would yield reduced RMS differences (see Table IV). In the limiting case, where the time average was over the entire data acquisition period, the RMS difference reduces to 0.06 m s^{-1} (i.e., 9.67–9.61 m s^{-1}).

Very good agreement is seen between the lidar and tower directions as shown in Figure 4. The mean difference in direction is approximately 2°. The lidar follows the abrupt changes in direction accurately with a 10 min RMS difference of approximately 19°. Similarly, longer averaging times would yield lower RMS differences. The reason for the discrepancy in measurement is most likely due to the spatial averaging performed by the lidar measurements and the differences in

Table II. Tower–lidar wind speed statistics over the period of observation.

Instrument	Mean (m s^{-1})	Standard deviation (m s^{-1})	10 min RMS difference (m s^{-1})
Tower at 50 m	9.67	3.60	1.18
Lidar at 50 m	9.61	3.61	

RMS = root mean square.

Table III. Tower–lidar direction statistics over the period of observation.

Instrument	Mean (deg)[a]	Standard deviation (deg)[a]	10 min RMS difference (deg)[a]
Tower at 50 m	168.24	36.94	19.40
Lidar at 50 m	170.34	37.01	

[a]Data utilized between 60–300°.
RMS = root mean square.

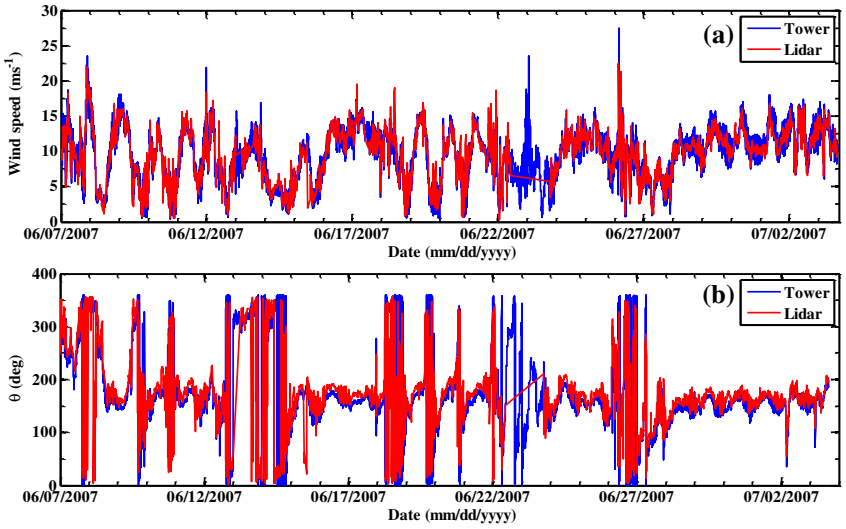

Figure 4. (a) Comparison between 1 min averaged tower and 10 min interpolated lidar wind speed at 50 m. (b) Comparison between 1 min averaged tower and 10 min interpolated lidar direction at 50 m. A total of 3459 ten minute periods are chosen for both figures. Gaps in the series correspond to bad signal-to-noise ratio at those time periods and hence was neglected.

Table IV. Wind speed RMS difference statistics for various time averaging periods.

Wind speed RMS difference	10 min RMS difference (m s^{-1})	1 h RMS difference (m s^{-1})	24 h RMS difference (m s^{-1})
At 50 m	1.18	0.72	0.46

RMS = root mean square.

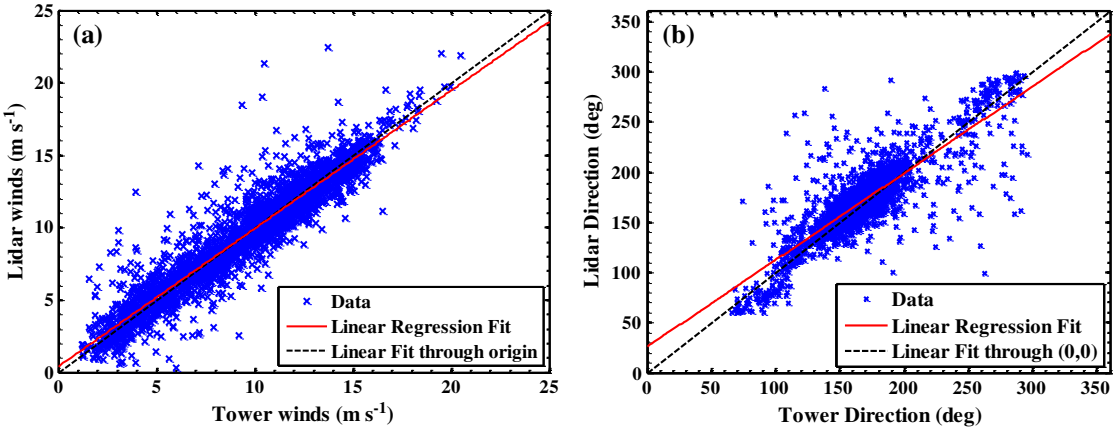

Figure 5. (a) Scatter plot of tower versus lidar wind speed at 50 m. Standard regression analyses produced the best fit line ($y = 0.95x + 0.4$) showing 94% correlation (solid line), and the linear fit through origin is also shown (dotted line). (b) Scatter plot of tower versus lidar wind direction at 50 m. Data are analyzed between directions 60–300°.

temporal averaging for the 10 min period. That is, the lidar obtains one stack of PPIs during this period, whereas the wind vanes collect data continuously at 2 Hz for each 10 min period. Scatter plots of lidar versus tower wind speed and direction are shown in Figure 5. Standard regression analyses resulted in a fit with 94% correlation. It was sometimes the case that the wind direction caused the lidar 'look-direction' toward the tower to be nearly perpendicular with respect to the mean flow direction. This created a more stringent test for the retrieval algorithm than if the tower had been more directly and consistently along the mean wind direction from the lidar. The scatter plot of lidar versus tower wind speed orthogonal to

the lidar mean wind direction (170°) is shown in Figure 6. Correlation between the tower and lidar measurements is 89%. U-component (N–S) and V-component (E–W) scatter plots between lidar and tower for the period of observation are shown in Figure 7. The correlation coefficient of the U component is approximately 95%, whereas the correlation coefficient for the V-component is calculated to be 88%. Spatially averaged lidar observations are a likely reason for the differences between tower and lidar. Figure 8 shows tower and lidar wind roses for the entire observation period. Each wind rose was divided into 12 directional sectors (30° per sector) with 5 m s^{-1} wind speed bins. Some effect of spatial averaging by lidar measurements can be observed in Figure 8, although generally the estimates from both lidar and the tower data are in relatively close agreement. This provides evidence of the accuracy of the retrieval algorithm applied to lidar data. Since only one tower was placed in the observation site, further validation could not be performed.

5. RESULTS

5.1. Terrain-following wind maps

One of the key advantages of 3D scanning coherent Doppler lidar is to generate wind maps on a terrain-following layer at hub height for the region of interest. The wind speed data were placed on a 12 km × 12 km grid domain and overlaid on

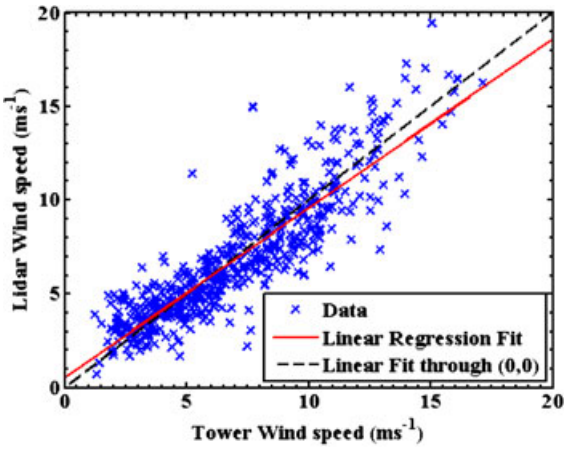

Figure 6. Scatter plot of tower versus lidar wind speed at orthogonal directions to mean wind direction (170° ± 45°) at 50 m. A linear regression fit ($y = 0.9x + 0.56$) showing 89% correlation (solid line) and the linear fit through origin (dotted line) are shown.

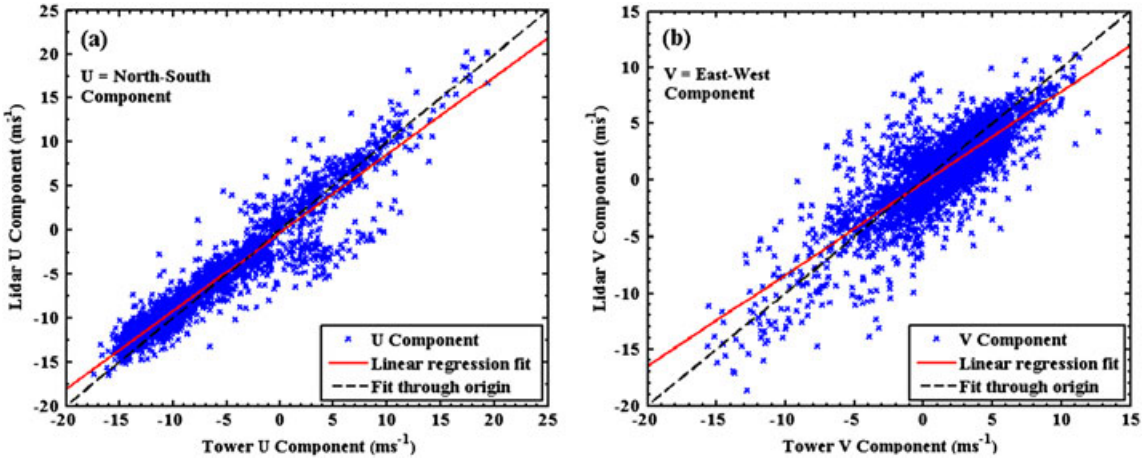

Figure 7. (a) U-component scatter plot of tower versus lidar at 50 m. A linear regression fit ($y = 0.89x - 0.27$) showing 96% correlation (solid line) and the linear fit through origin are shown (dotted line). (b) V-component scatter plot of tower versus lidar at 50 m. A linear regression fit ($y = 0.81x - 0.2$) showing 88% correlation (solid line) and the linear fit through origin (dotted line) are shown.

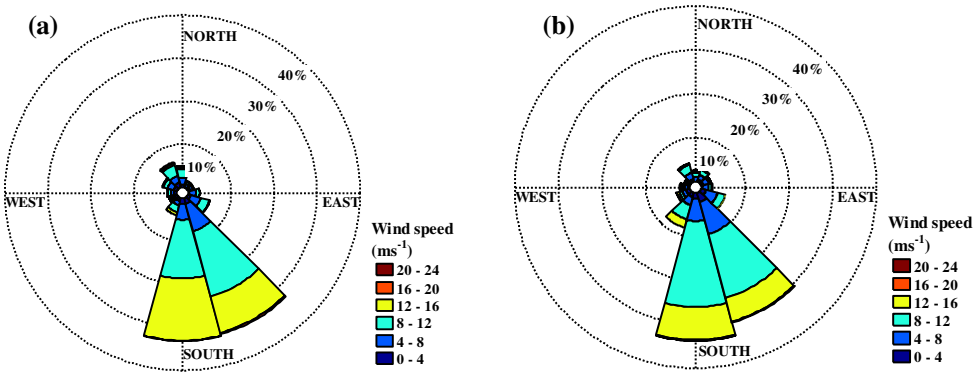

Figure 8. (a) Tower wind rose for the period of observation at 50 m. (b) Lidar wind rose for the period of observation at 50 m. Wind speeds (six bins of 5 m s^{-1}) were divided into 12 directional sectors. Percentage circles (10, 20, 30 and 40%) are also shown.

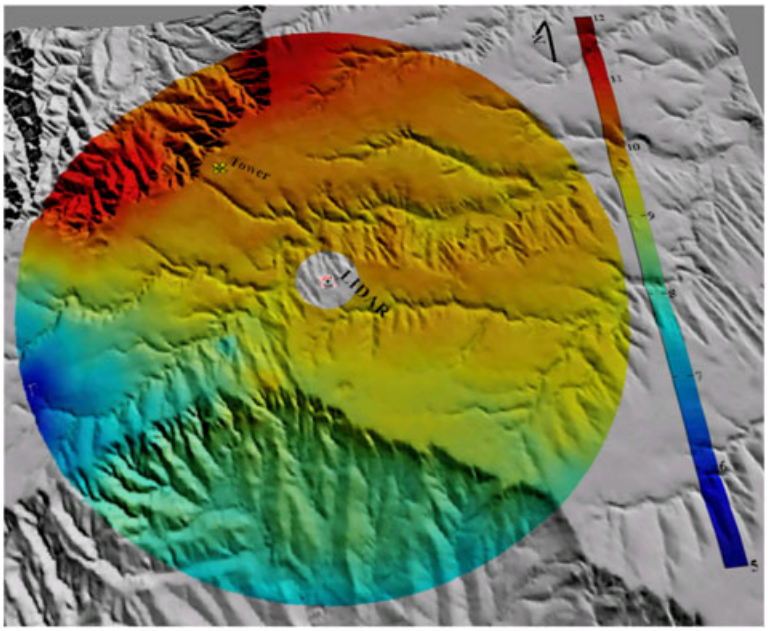

Figure 9. Lidar terrain-following averaged wind speed measurement at 80 m hub height. The color bar represents wind speed from 5 to 12 m s^{-1}. The lidar is at the center, and the tower is located 3.42 km northwest of the lidar. The radius of the scan is 5.75 km.

a digital terrain model. The resultant map covers a geographic area of 144 km^2 and is composed of approximately 9150 data points on the terrain-following plane. Figure 9 shows the 3D image of the terrain-following wind field at 80 m hub height. Such spatially resolved wind maps (on terrain-following surfaces at hub height) may aid developers to gain more complete understanding of the spatial variation of winds within a prospective wind farm. On the basis of visual inspection of the wind map, it is straightforward to locate the area with maximum winds. It can be observed from Figure 9 that for the period of observation, maximum mean wind speeds of greater than 12 m s^{-1} are observed near the northwestern ridges and minimum winds up to 5 m s^{-1} are observed near the southwestern section of the domain. For this site, locations near the northern ridge and on the western side of the plateau would result in maximum wind power production. Analyzing many days of lidar data, it was found that the winds in this region tend to channel across the northern ridge. Although the mean wind direction at hub height is approximately from the south, rapid changes in wind direction and wind shear are observed for many days and could be of interest for wind farm developers. Therefore, an advanced optimal interpolation velocity retrieval algorithm has been applied to the lidar data to characterize abrupt changes in wind direction, and one such event is presented in Section 5.7 of this paper.

5.2. Wind distributions

Of course, the energy content of the wind depends not only on the mean wind speed but also on wind speed distribution. Lidar is capable of providing wind speed distributions at every point over the entire spatial domain. Evidence is provided for two hypotheses:

- Modern 3D-scanning lidar can measure accurate wind speed distributions over large areas from one central location.
- The wind speed distribution can be strong functions of spatial position, especially for wind farms in or near complex terrain.

The distribution of the winds from the tower is compared with those estimated from the lidar at the tower location. Since the cup anemometers on the tower are located at a height of 50 m (AGL), the lidar data were interpolated to this height, as given in Section 4, and the distributions are compared. The winds measured on a terrain-following surface at 50 m are binned into 30 wind speed categories, allowing estimation of the wind speed distribution. As observed in Figure 10(a), tower and lidar distributions compare reasonably well. Radial and transverse wind speed distributions between lidar and tower are compared in Figure 10(b),(c), respectively. For the wind speed distributions in radial and transverse directions to be calculated, wind speeds were binned into four 90° sectors on the basis of the wind speed directions: two sectors along the radial direction, i.e., $170 \pm 45°$ and $350 \pm 45°$, and two sectors along the transverse direction, i.e., $80 \pm 45°$ and $260 \pm 45°$. The distributions in the transverse directions are less converged because of insufficient data points observed in the two sectors. The lidar wind speed distributions in radial and transverse direction compare reasonably well with tower distributions.

For the variation of winds with height to be understood, the distributions at various vertical levels within the rotor swept area have also been analyzed. In Figure 11, the distributions from lidar at 50, 80 and 110 m (AGL) are compared. A more apparent bimodal distribution is observed at higher elevations. The lower mode is at approximately 4–7 m s^{-1}, and the upper mode is approximately at 10 m s^{-1}.

On the basis of lidar estimates, it can be observed that different distributions are obtained at various locations (three) within the region (Figure 12). The locations shown as cross marks (x) in Figure 1 observed different wind speed distributions. The energy estimated by each of these distributions varies significantly. These measurements could be used to estimate the error from current mesoscale, computational fluid dynamics and linear wind resource prediction models (such as Wind Atlas Analysis and Application Program, etc.).[39]

5.3. Diurnal variation of wind speed

Two-hour averaged vertical profiles of wind speeds for the entire period of observation is shown in Figure 13. As it can be observed from Figure 13, diurnal variations are prominent at this site (during the observation period). Higher gradients of

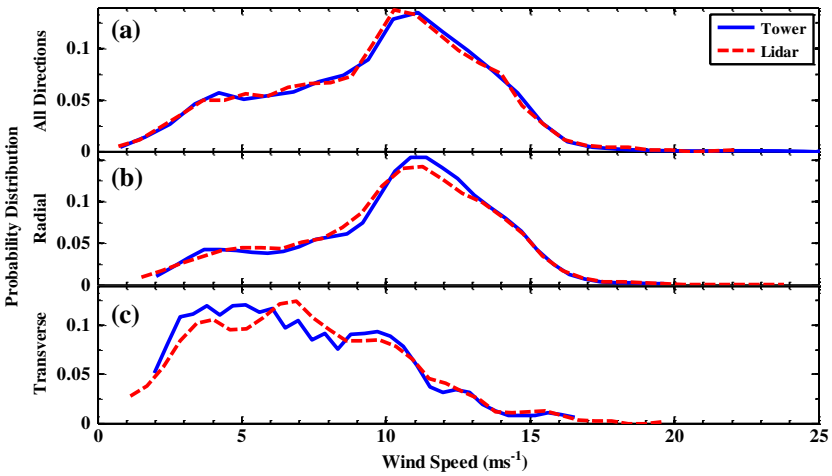

Figure 10. (a) Distribution of wind speed comparison between tower and lidar measurements at 50 m (from all directions). (b) Wind speed distribution between the tower and the lidar in the radial direction at 50 m. Wind speed data selected from directions $170 \pm 45°$ and $350 \pm 45°$ were chosen for this distribution (mean wind direction is 170°). (c) Wind speed distribution between the tower and the lidar in the transverse direction at 50 m. Wind speed data selected from directions $80 \pm 45°$ and $260 \pm 45°$ were chosen for the distribution (mean wind direction is 170°). The distribution is less well defined because of reduced amount of data perpendicular to the mean wind direction.

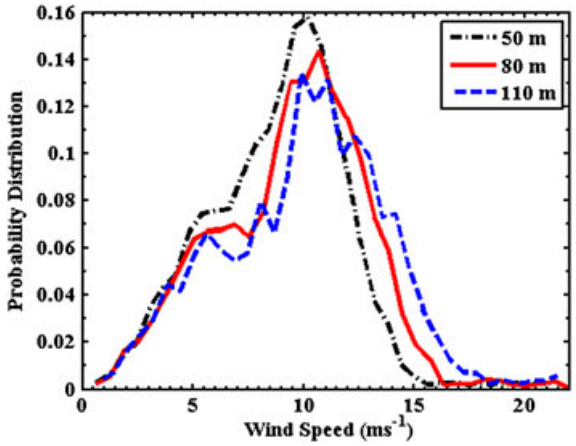

Figure 11. Distribution of wind speed from lidar at three vertical levels within the turbine rotor region from lidar measurements, showing bimodal distribution (i.e., one peak near 5–7 m s^{-1} and another at 10 m s^{-1}) at 50, 80 and 110 m heights (from all directions).

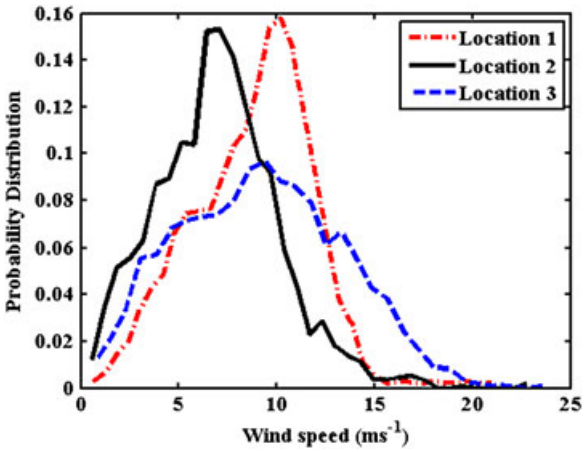

Figure 12. Different distribution of wind speed observed at various locations from lidar measurements, 50 m above ground level (from all directions). Locations 1, 2 and 3 are shown in Figure 1.

wind speed are observed during night time, and more neutral conditions are observed in the middle of the day. During day time, the average wind speed increase, for 60 m height difference, is less than 0.5 m s^{-1}. On the other hand, during night time, average wind speeds are observed to change from 10 to 12.5 m s^{-1} for the same height difference. Figure 13 shows that a small change in turbine hub height at the site could result in significant net increase or decrease of power production.

5.4. Wind power production

The wind resource or wind power production for a particular site can be estimated based on wind speed distribution for the given area. As shown in the previous section, the distribution of winds over the entire site has been measured. The wind power production for a specific turbine site can be calculated using the *average wind machine power*, given by equation 4.[40]

$$\bar{P}_w = \frac{1}{N} \sum_{j=1}^{N_B} P_w(m_j) f_j \tag{4}$$

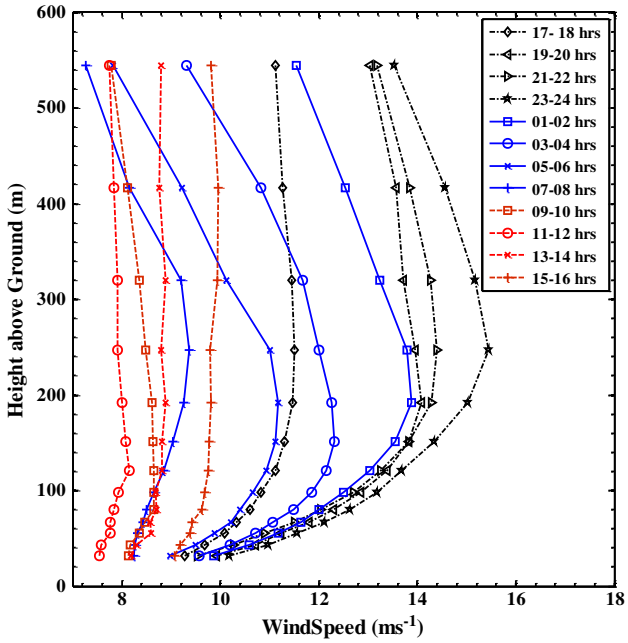

Figure 13. Monthly 2 h averaged vertical profiles of wind speed for 24 h (data collected 3 km north of the site) showing strong diurnal variations from lidar measurements. The legend displays local times.

where N_B are the number of bins used in the distribution, m_j are the midpoints of each of those bins, f_i are the number of occurrences in each bin or frequency, such that

$$N = \sum_{j=1}^{N_B} f_j$$

and $P_w(U)$ is the power output defined by the particular wind machine power curve at velocity U.

The total energy output is calculated at every location at hub height on the basis of the distribution of wind speed and the power curve (assuming a standard 80 m hub 2.1 MW wind turbine power curve). Figure 14 shows the average machine power on a terrain-following surface at hub height. It should be noted that the errors normally associated with scaling the wind speed distribution from the meteorological tower by a linear factor calculated by a wind flow model (such as Wind Atlas Analysis and Application Program), or using Weibull, Rayliegh distribution, etc., are avoided, therefore providing an estimate of the wind power density based purely on measurements.[40]

5.5. Wind farm layout design

Even though the length of the deployment reported on herein was much too short to be considered climatological, a simple model for turbine placement and wind farm design was explored for demonstration purposes. This section is based on lidar-derived total machine power output. The turbine locations are roughly placed on the basis of maximum machine power output estimated from lidar and a constant $10D$ (where D is the diameter of the turbine) turbine spacing. This demonstration demo is based purely on lidar measurement, and different layout designs can be evaluated on the basis of the constraints applied. A simple approach such as this could be used as an initial estimate for advanced optimization techniques.

The assumptions used for wind farm layout design are presented in the following.

Assumption 1. Two-dimensional Cartesian grids (x, y) of size 90 m × 90 m are overlaid over the polar grid cells (measured by the lidar). This assumption implies that there is negligible variation of the surface roughness within a polar coordinate grid cell. The solution estimated in this paper is represented by N Cartesian coordinates (x_i, y_i), $i = 1 \ldots N$, where N is the number of wind turbines for the given project.

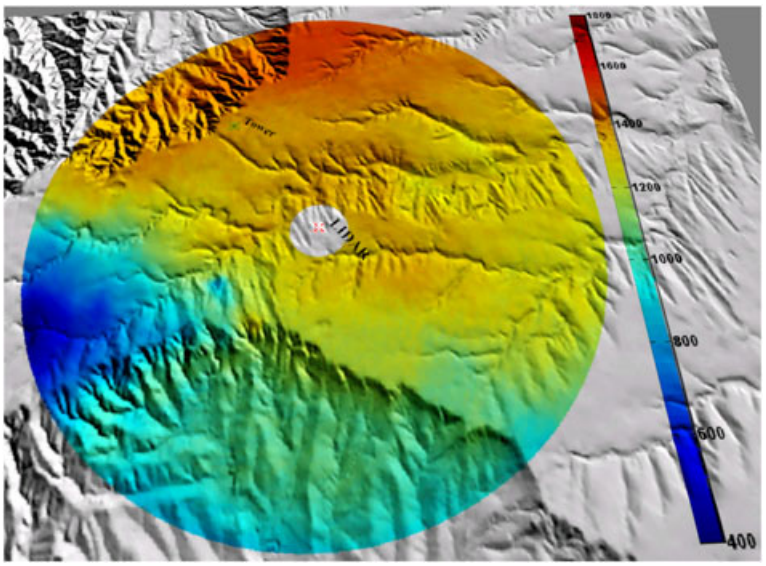

Figure 14. Lidar terrain-following machine power production at 80 m hub height. The color bar represents the power in kilowatt.

Assumption 2. All wind turbines are assumed to have the same power curve function. The total yield can be estimated on the basis of the distribution of wind speed at every location (on the grid at hub height) and the assumed power curve. The period of observation is assumed to be representative of longer periods, for the purposes of this demonstration. Also, the wind turbine is assumed to be oriented perpendicular to the mean wind direction at any given period of time.

Assumption 3. Any two turbines in a wind farm are separated from each other by at least 10 rotor diameters. This constraint attempts to ensure that wind profiles have recovered sufficient energy before interaction with another turbine. Therefore, given the rotor diameter D, the distance between two adjacent turbines $(x_\mathrm{i}, y_\mathrm{i})$ and $(x_\mathrm{j}, y_\mathrm{j})$ should satisfy the inequality $(\mathrm{x_i} - \mathrm{x_j})^2 + (\mathrm{y_i} - \mathrm{y_j})^2 \geq 100D^2$. This assumption is based on rules of thumb from the industry.[41] Additional constraints could be placed on the distance between each turbines on the basis of the wind direction but are not in this demonstration design process.

An example placement of wind turbines based on machine power density subject to the distance constraints (for 75 wind turbines) is shown in Figure 15. Once the turbine locations were found, a simple topology gradient algorithm was run to pick the highest terrain location within 200 m of each turbine. The turbines are shifted to the new location, approximately maintaining the distance constraint. Such a product could provide an initial estimate for the total yield produced by the wind farm or an input to global optimization algorithms, if the observational time was made suitably long or long-term meteorological adjustments were made on the basis of a correlation with a reference station.

5.6. Layered approach

For the power output from a turbine to be estimated, it is a general practice to assume that the mean wind speed at hub height is representative of the wind over the whole swept area. Since greater wind speeds and shear are often observed at the higher elevations associated with the largest wind turbines, there may be significant differences in wind speed within the rotor swept area. If these variations in the wind profile (and their associated extractable energy) are not well represented by a single measured value at hub height, significant errors could be introduced into estimates of power production.[15] Therefore, since the measured lidar data present the opportunity to analyze winds at a variety of vertical levels within the rotor swept area, an analysis using multiple vertical layers is explored. The approach of Wagner *et al.*[15] is followed, where terrain-following average wind power is estimated using equation 5 at various vertical levels within the swept rotor area. The combined wind power from all the layers is estimated by equation 6.

$$\bar{P}_{wl} = \frac{1}{2}\rho\overline{U}^3 \tag{5}$$

$$\bar{P}_{wc} = \frac{1}{2}\rho\sum_i \overline{U}_i^3 \frac{A_i}{A} \tag{6}$$

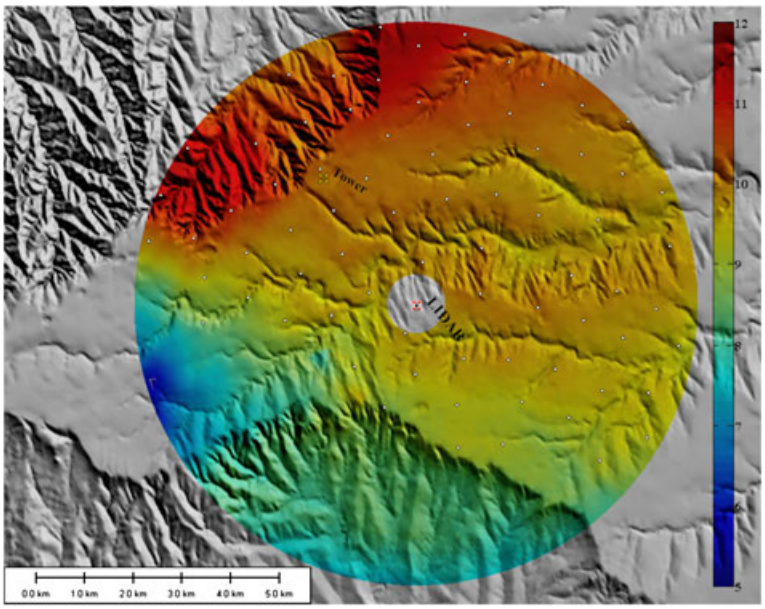

Figure 15. Optimal locations of wind turbines (75) overlaid over averaged wind map. The white circular dots represent locations of wind turbines based on the algorithm. The color bar shows wind speed in meter per second at 80 m hub height.

where $\bar{P}_{wl}$ is the wind power density at each layer, $\bar{P}_{wc}$ is the combined wind power density from all layers, ρ is the density of air (1.225 kg m^{-3}), A is the total area of the rotor, A_i is the area of winds covered by each layer ($i = 1, 2$ and $3) = A/3$, and $\overline{U}$ is the average 10 min wind speed estimates at different vertical levels.

In this paper, three layers (50, 80 and 110 m AGL) were chosen, and the area covered by each layer was equally divided. Figure 16 shows the available wind power density estimated at the three individual layers and combined wind power density (all three layers together.) As observed in Figure 16, the power density changes significantly among the layers as well as the combined approach. Table V shows the ratio of the mean wind power density estimated at different layers (50 m, 110 m and combined) by the wind power density at hub height. The mean wind power for the entire layer (terrain-following wind map) estimated at hub height (80 m) is under-predicted by 0.05% compared with the combined layer wind power. Although

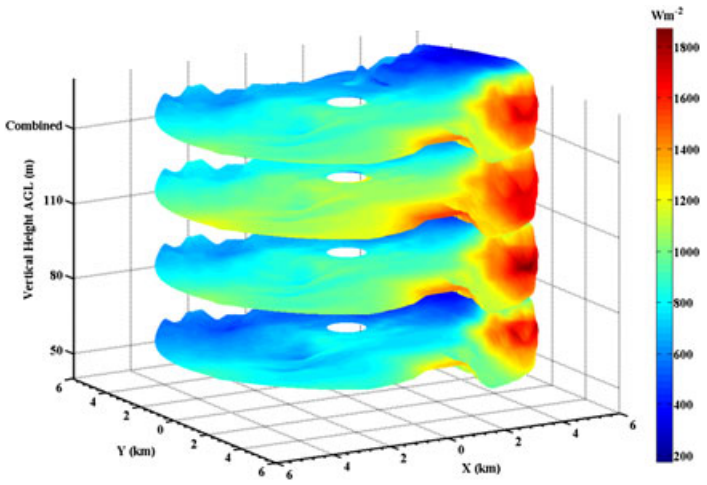

Figure 16. Terrain-following wind power density estimates at various heights of the rotor swept area. The 'combined' wind power density estimated from all the three layers is also shown, where X (km) and Y (km) are the distances from lidar in the respective directions.

Table V. Percent change in wind power density estimates at various layers with respect to hub height.

Layer height AGL (m)	Change in mean power density with respect to 80 m hub height (%)[a]
50	−16.42 (↓)
110	16.59 (↑)
Combined[b]	0.054 (↑)

[a]Based on wind power density at 80 m hub height.
[b]Combined—total wind power estimated based on all three layers together.
AGL = above ground level.

the wind power difference between the layers is small in this case, the potential to measure the expected energy through the entire layer has been demonstrated. However, the wind power that would be extracted at the chosen turbine locations (from Section 5.5) at hub height is underestimated by 0.49% compared with the estimated combined layer wind power at the turbine locations. Therefore, predicting the wind power based solely on the mean winds at hub height for a wind farm may include a degree of error associated with insufficient representation of wind profile variations in the vertical. Increasing the number of layers would most likely provide a more realistic estimate of the total wind power potential of this site, although larger vertical interpolation is performed at farther range gates due to diverging lidar beams.

5.7. Investigation of vector retrieval methods

The wind energy methods given previously depend upon the accuracy and degree of suitability of the vector retrieval methods for the domains of interest. Evidence is presented in this paper that the VVP method produces results that compare

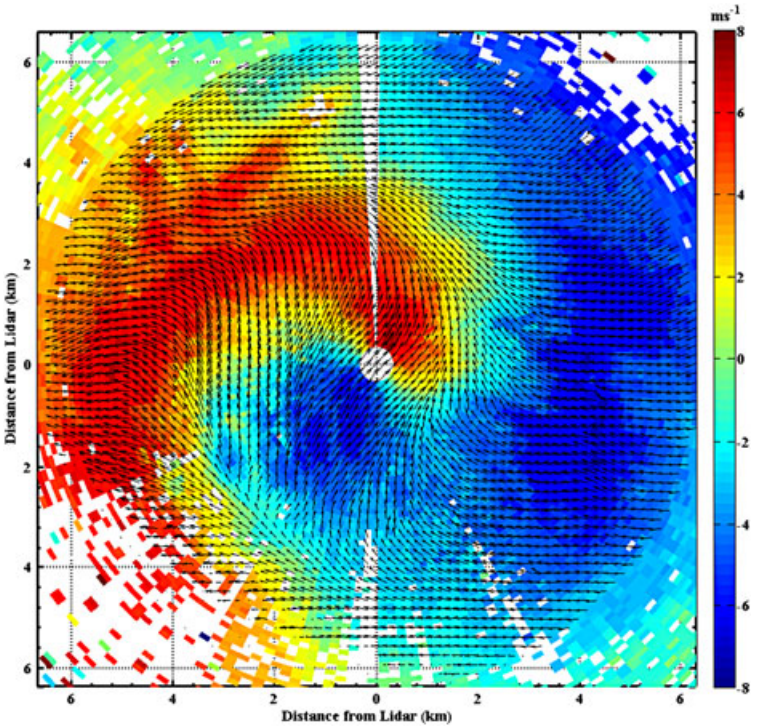

Figure 17. Horizontal velocity vectors from optimal interpolation technique on a 3.5° elevation conical scan showing the rotation of winds with height. The scan takes approximately 38 s to complete one revolution shown. The colors on the plot represent radial velocity measurements by lidar. Red color (positive values) represents wind moving away from the lidar, and blue color (negative values) shows wind moving towards the lidar. Data with low signal-to-noise ratio are not shown (white regions).

well with tower data for this specific site and period of observation. However, more investigation of vector retrieval algorithms is recommended to more fully define error characteristics and to broaden options for application in conditions for which assumptions such as homogeneity over relatively large sectors may be less valid. Optimal interpolation methods (see Section 3.2) have been applied to Doppler lidar data and are designed to preserve more local variation in wind vectors. An example of this type of vector retrieval that has been applied to the dataset studied previously is given in Figure 17. It is expected that different uses of 3D scanning Doppler lidar, which may focus on more transient or more highly localized flow features, may require more advanced vector retrieval methods.

6. SUMMARY

A Doppler lidar was used to obtain radial velocities over a wind farm domain. Mean wind speeds were obtained on a terrain-following surface at hub height. The wind speed distributions were shown to be obtainable with reasonable accuracy with the given algorithms. For this site, the wind speed distribution was shown to vary significantly with spatial location. Therefore, a key result of this study is that (spatially varying) mean wind speeds and their distributions can be *measured* from one central location in the wind farm—although an important caveat is that more experimental data are required to fully define and understand the error structure of the products, particularly in the regions of the domain perpendicular to the mean wind. Field experiments that also deploy instruments capable of measuring winds and their distributions at multiple heights in the off-mean-wind direction would be a valuable next step for validating scanning Doppler lidar products for wind energy.

As a demonstration, an example wind farm layout was designed to maximize power subject to several simple constraints. 3D Doppler lidar data can be used to produce 'layered' wind and power estimates, accounting for wind variations at different elevations of the rotor swept area. The algorithmic keystone of these methods is the vector retrieval algorithm, and new methods such as those utilizing an optimal interpolation framework are briefly described. Future work will focus on characterizing errors associated with lidar measurements and their retrieval algorithms for wind speed estimates.

ACKNOWLEDGEMENTS

The authors recognize the support of the ONR Summer Faculty Program (NRL Host: Dr. James Doyle), in which one of the authors spent a summer at the Naval Research Laboratory in Monterey, CA, USA. Support was also provided through the Army Research Office, sponsor awards W911NF0410146 and W911NF0710137 (Program Officer: Walter Bach) and the NSF grant 0522307 (Program Officer: Stephan P. Nelson), which made this work possible. The authors also thank all the reviewers of the journal for their valuable input on the paper.

REFERENCES

1. AWEA, 2010. http://www.awea.org.
2. Amar FB, Elamouri M, Dhifaoui R. Energy assessment of the first wind farm section of Sidi Daoud, Tunisia. *Renewable Energy* 2008; **33**: 2311–2321.
3. Belu R, Koracin D. Wind characteristics and wind energy potential in western Nevada. *Renewable Energy* 2009; **34**: 2246–2251.
4. Hannon SM, Barr K, Novotny J, Bass J, Oliver A, Anderson M. Large scale wind resource mapping using a state-of-the-art 3-D scanning lidar, *European Wind Energy Conference*, 2008.
5. Mikkelsen T, Mann J, Courtney M. Windscanner: a full-scale laser facility for wind and turbulence measurements around large wind turbines, *European Wind Energy Conference*, Brussels (BE), 31 March - 3 April, 2008.
6. Smith DA, Harris M, Coffey AS, Mikkelsen T, JØrgensen HE, Mann J, Danielian R. Wind LIDAR evaluation at the Danish wind test site in HØvsØre. *Wind Energy* 2006; **9**: 87–93.
7. Bingöl F, Mann J, Larsen GC. Light detection and ranging measurements of wake dynamics, part I: one-dimensional scanning. *Wind Energy* 2010; **13**: 51–61.
8. Barthelmie R, Folkerts L, Larsen G, Pryor SC, Frandsen ST, Schepers G. Comparison of wake model simulations with offshore wind turbine wake profiles measured by sodar. *Journal of Atmospheric and Oceanic Technology* 2006; **23**(7): 888–901.
9. Gal-chen T, Xu M, Eberhard W. Estimations of atmospheric boundary layer fluxes and other turbulence parameters from Doppler lidar data. *Journal of Geophysical Research* 1992; **97**: 409–418.
10. Newsom R, Ligon D, Calhoun R, Heap R, Cregan E, Princevac M. Retrieval of microscale wind and temperature fields from single- and dual-Doppler lidar data. *Journal of Applied Meteorology* 2005; **44**(9): 1324–1345.

11. Frehlich R, Hannon S, Henderson S. Coherent Doppler lidar measurements of wind field statistics. *Boundary-Layer Meteorology* 1998; **86**: 233–256.
12. Retallack C, Calhoun R, Fernando HJS, Rayner K, Stuart A, Sutton J, Hibberd MF. Flow and pollution transport during Wagerup 2006: a case study. *Meteorological Applications* 2010; **17**: 269–278. DOI: 10.1002/met.161.
13. Laks JH, Pao LY, Wright A. Control of wind turbines: past, present, and future, *Proceedings of American Control Conference*, St. Louis, MO, 2009.
14. Käsler Y, Rahm S, Simmet R, Kühn M. Wake measurements of a multi-MW wind turbine with coherent long-range pulsed doppler wind lidar. *Journal of Atmospheric and Oceanic Technology* 2010; **27**(9): 1529–1532.
15. Wagner R, Antoniou I, Pedersen SM, Courtney MS, Jørgensen HE. The influence of the wind speed profile on wind turbine performance measurements. *Wind Energy* 2009; **12**: 348–362. DOI: 10.1002/we.297.
16. Banta RM, Newsom RK, Lundquist JK, Pichugina YL, Coulter RL, Mahrt L. Nocturnal lowlevel jet characteristics over Kansas during CASES-99. *Boundary-Layer Meteorology* 2002; **105**: 221–252.
17. Banta RM, Pichugina YL, Kelley ND, Jonkman B, Brewer WA. Doppler lidar measurements of the great plains low-level jet: applications to wind energy, *14^{th} International Symposium for the advancement of Boundary Layer Remote Sensing*, 2008.
18. Chan PW, Shao AM. Depiction of complex airflow near Hong Kong International Airport using a Doppler LIDAR with a two-dimensional wind retrieval technique. *Meteorologische Zeitschrift* 2007; **16**: 491–504.
19. Lin C, Xia Q, Calhoun R. Retrieval of urban boundary layer structures from Doppler lidar data. Part II: proper orthogonal decomposition. *Journal of Atmospheric Sciences* 2008; **65**(1): 21–42.
20. Xia Q, Lin C, Calhoun R, Newsom R. Retrieval of urban boundary layer structures from Doppler lidar data. Part I: accuracy assessment. *Journal of Atmospheric Sciences* 2008; **65**(1): 3–20.
21. Kongara S, Calhoun R, Choukulkar A, Boldi M. Velocity retrieval for coherent Doppler lidar. *International Journal of Remote Sensing* 2011; In Press.
22. Doviak RJ, Zrnic DS. *Doppler Radar and Weather Observations*, 2nd ed. Academic Press, 1993, 304 pp.
23. Calhoun R, Heap R, Princevac M, Newsom R, Fernando H, Ligon D. Virtual towers using coherent Doppler lidar during the Joint Urban 2003 Experiment. *Journal of Applied Meteorology* 2006; **45**: 1116–1126.
24. Newsom R, Calhoun R, Ligon R, Allwine J. Linearly organized turbulence structures observed over a suburban area by dual-Doppler lidar. *Boundary-Layer Meteorology* 2008; **127**(1): 111–130.
25. Drechsel S, Chong M, Mayr G, Weissmann M, Calhoun R, Dörnbrack A. Three-dimensional wind retrieval: application of MUSCAT to dual Doppler lidar. *Journal of Atmospheric and Oceanic Technology* 2009; **26**(3): 635–646.
26. Hill M, Calhoun R, Fernando H, Wieser A, Dörnbrack A, Weissmann M, Mayr G, Newsom R. Coplanar Doppler lidar retrieval of rotors from T-REX. *Journal of the Atmospheric Sciences* 2010; **67**(3): 713–729.
27. Henderson SW, Hale CP, Magee JR, Kavaya MJ, Huffaker AV. Eye-safe coherent laser radar system at 2.1 μm using Tm, Ho:YAG lasers. *Optics Letters* 1991; **16**: 773–775.
28. Henderson SW, Suni PJM, Hale CP, Hannon SM, Magee JR, Bruns DL, Yuen EH. Coherent laser radar at 2 _m using solid-state lasers. *IEEE Transactions of Geoscience and Remote Sensing Society* 1993; **31**(1): 4–15.
29. Waldteufel P, Corbin H. On the analysis of single-Doppler radar data. *Journal of Applied Meteorology* 1979; **18**: 532–542.
30. Xin L, Reuter WG. VVP technique applied to an Alberta storm. *Journal of Atmospheric and Oceanic Technology* 1997; **15**: 587–592.
31. Boccippio DJ. A diagnostic analysis of the VVP single-Doppler retrieval technique. *Journal of Atmospheric and Oceanic Technology* 1995; **12**: 230–248.
32. Xu Q, Liu S, Xue M. Background error covariance functions for velocity wind analysis using Doppler radar radial-velocity observations. *Quarterly Journal of the Royal Meteorological Society* 2006; **132**: 2887–2904.
33. Xu Q, Nai K, Wei L. An innovation method for estimating radar radial-velocity observation error and background error covariances. *Quarterly Journal of the Royal Meteorological Society* 2007; **133**: 407–415.
34. Xu Q, Gong J. Background error covariance functions for Doppler radial-wind analysis. *Quarterly Journal of the Royal Meteorological Society* 2003; **129**: 1703–1720.
35. Lorenc A. A Global three dimensional multivariate statistical analysis system. *Monthly Weather Review* 1981; **109**: 701–721.
36. Daley R. *Atmospheric Data Analysis*. Cambridge University Press: New York, 1991.
37. Browning KA, Wexler R. The determination of kinematic properties of a wind field using Doppler radar. *Journal of Applied Meteorology* 1968; **7**: 105–113.

38. Peterson EW, Hennessey JP. On the use of power laws for estimates of wind power potential. *Journal of Applied Meteorology* 1978; **17**: 390–394.
39. Sempreviva A, Barthelmie R, Pryor S. Review of methodologies for offshore wind resource assessment in European seas. *Surveys in Geophysics* 2008; **29**: 471–497.
40. García-Bustamante E, González-Rouco JF, Jiménez PA, Navarro J, Montávez JP. The influence of the Weibull assumption in monthly wind energy estimation. *Wind Energy* 2008; **11**: 483–502. DOI: 10.1002/we.270.
41. Manwell JF, McGowan JG, Rogers AL. *Wind energy explained: theory, design and application*. John Wiley & Sons: London, 2009.